ARTICLES

Nonlinear unstable viscous fingers in Hele–Shaw flows. II. Numerical simulation

E. Meiburg and G. M. Homsy

Department of Chemical Engineering, Stanford University, Stanford, California 94305

The nonlinear stages of two-dimensional immiscible displacement processes in Hele–Shaw flows are investigated by means of large scale numerical simulations based on a purely Lagrangian vortex method. The vortex sheet at the interface between the two fluid phases is discretized into circular arcs with a continuous distribution of circulation, which renders our numerical technique highly accurate. A complicated unsteady growth mechanism is observed for the emerging viscous fingers, involving a combination of spreading, shielding, and tip splitting. As the surface tension is further reduced, smaller length scales arise and the fingertip exhibits a new splitting pattern in which three new lobes emerge instead of two. Monitoring the velocity as well as the radius of curvature at the fingertip demonstrates that the instability of the finger evolves in an oscillatory fashion. The two-lobe and the three-lobe splitting can thus be explained as different manifestations of the same instability mode. Comparison with experiment shows good qualitative but only fair quantitative agreement. By imposing a constraint on the curvature at the fingertip, experimental results, which show fingers of width considerably smaller than half the cell width and exhibit "dendritic" instability modes, are reproduced.

I. INTRODUCTION

The unstable character of flows in which a less viscous fluid displaces a more viscous one was recognized long ago (Hill[1]). Chuoke, van Meurs, and van der Poel[2] as well as Saffman and Taylor[3] carried out the linear stability analysis for immiscible flow and showed how the surface tension at the interface determines the length scale of the problem. More recently, the subject of viscous fingering has been the focus of numerous experimental and theoretical investigations, the motivation originally stemming from its relevance to certain enhanced oil recovery schemes (for a review, see Wooding and Morel-Seytoux[4]). However, both the nonlinear growth patterns observed for small values of surface tension and the stability calculations regarding a single steady finger and its width as a function of surface tension have emerged as challenging problems in their own right. Reviews on these rapidly evolving topics can be found in Saffman[5] and Homsy[6]. Park and Homsy[7] showed experimentally that viscous fingers are subject to a tip-splitting instability for high flow rates. Subsequently, Maxworthy[8] studied an even more unstable configuration, suggesting that the resulting interface develops in a self-similar fashion and thus might be of fractal dimension.

Kopf-Sill and Homsy[9] observed a new kind of instability at the fingertip, a splitting process that results in three new lobes instead of two as seen in previous experiments. This finding is surprising insofar as the tip evolves fundamentally differently in the two splitting scenarios: while in the two-lobe splitting mode it slows down and eventually stops advancing altogether, during the three-lobe splitting it accelerates and remains the most advanced part of the finger. Couder, Gerard, and Rabaud[10] as well as Couder *et al*.[11] placed a small bubble at the fingertip and investigated the effect of the resulting small perturbation on the evolution of the finger. They find that the fingertip no longer splits and observe a different kind of instability instead, which leads to a dendritic growth of a single finger. Recently, Kopf-Sill and Homsy[12] experimentally found narrow fingers of only about one-sixth of the cell width even without any kind of artificial perturbation. They furthermore observed dendritic instability of these narrow fingers. These fingers were observed for very clean conditions and might indicate a second family of solutions to the Hele–Shaw equations, although a complete understanding of them has not yet been achieved.

Motivated by these observations, we address the question as to how the finger instability develops, and what determines which modes occur. Accurate numerical simulations promise to be of some help in investigating these questions, since they allow a more detailed monitoring of such local quantities as the tip radius of curvature and tip velocity than can be achieved by flow visualization. Since for moderate to low values of the dimensionless surface tension, two-phase flows in a Hele–Shaw cell are already affected by three-dimensional effects (Park and Homsy,[13] Tabeling, Zocchi, and Libchaber,[14] and Reinelt[15]), it is not clear *a priori* that all the effects mentioned above actually arise as solutions to the Hele–Shaw equations, which are obtained by averaging over the gap width. Numerical simulations based on the Hele–Shaw equations can provide some additional information on this subject.

The above-mentioned experiments by Couder *et al.*,[10,11] as well as recent theoretical investigations,[16–19] indicate the importance of the narrow region around the fingertip for the global features of the flow. Small perturbations located there can significantly alter the global behavior of fingers as well as their stability characteristics. The question of how a small

perturbation at the tip can change the global flow again draws attention to the role the tip itself plays during the evolution of the instability of the finger. In this context, the relevance of cusps, i.e., points on the interface where the radius of curvature is undefined, is currently being discussed.[16-19]

The above goals imply that we need a numerical method of high accuracy. For the problem under investigation, front tracking techniques are advantageous. DeGregoria and Schwartz[20] employ a boundary integral method that maps the interface onto a closed curve and discretizes it into straight-line segments of sources of piecewise constant strength. Basing the discretization on the local values of the dimensionless surface tension, they are able to qualitatively reproduce the experimentally observed tip-splitting instability. Recently, they have reported the simulation of quasi-steady-state fingers with a width of approximately 6% less than half the cell width for low values of the surface tension.[21] In this regime, they also observe multiple solution tracks for the width of the fingers as a function of surface tension. In between these tracks they do not observe steady-state fingers, and instead their simulations lead to tip splitting. However, the discretization of the interface into straight-line segments has the effect of generating local discontinuities in curvature where these segments join. As pointed out by Hong and Langer,[16] the presence of cusps, which would be smoothed out in the real flow by surface tension, might allow stable fingers to form with a width of less than one-half the cell width. Consequently, we have developed a purely Lagrangian method based on the vorticity variable and discretize the interface into circular arcs (Meiburg and Homsy[22]). Although still present, the jumps in interface slope and curvature at those locations where two of the arcs join are thus minimized.

The organization of the paper is as follows: The numerical technique and test calculations will be presented in some detail in Sec. II. In Sec. III the results of our numerical simulations are reported. We will describe simulations of "naturally" growing fingers exhibiting the two experimentally observed instability modes. A detailed investigation of how the instability evolves will follow, revealing the two- and three-lobe splitting as variants of the same basic instability. In this way, the apparent contradiction of opposite behavior of the tip in the two cases is resolved. Subsequently, we will present results for fingers whose tip radius is artificially held constant, thus simulating the experiments in which a bubble was placed at the fingertip. As in the experiment, we will see that this small perturbation leads to increased stability of the finger, which becomes understandable in the light of the previous discussion of the role of the fingertip in the evolution of the instability. We will present fingers that grow in a dendritic fashion for low values of the dimensionless surface tension. In Sec. IV we will discuss our work in the context of other researcher's findings.

II. FORMULATION

A. Basic equations

Our goal is to numerically simulate two-phase flows in a Hele–Shaw cell. Initially, the gap between the two plates is filled with a fluid of dynamic viscosity μ_2. This fluid is to be displaced by injecting a fluid of viscosity μ_1. Here u_0 is the average velocity with which fluid 1 is injected. The width of the cell in the large, spanwise dimension is assumed to be $2L$, whereas the width of the gap in the small, transverse dimension is b. Both fluids are considered incompressible,

$$\nabla \cdot \mathbf{u} = 0 .$$

Within each phase, the dynamics of the two-dimensional flow field, averaged over the gap, is governed by a balance of pressure and viscous forces as expressed by the Hele–Shaw equations. For an immiscible two-phase flow we have to consider surface tension forces. By a local analysis of the three-dimensional effects at the interface,[13] we obtain as a first approximation for the conservation of momentum,

$$\nabla p = - (12\mu/b^2)\mathbf{u} - \mathbf{n}\delta(\mathbf{x} - \mathbf{x}_t(s)) \cdot [\sigma/R(s)] . \quad (1)$$

Here $\mathbf{x}$ denotes a position vector, with $\mathbf{x}_t$ representing the interface characterized by the arclength parameter s, $\mathbf{u}$ is the velocity vector, p is the pressure, and σ is a constant related to the surface tension and the contact angle in the transverse direction. It will be simply referred to here as "the surface tension." Here R denotes the local radius of curvature of the interface in the plane of the apparatus and $\mathbf{n}$ the outer normal to the interface (Fig. 1). The fact that surface tension forces act only at the interface itself is accounted for by the δ function. Equation (1) holds asymptotically in the limit $\mu_2 u_0/\sigma \to 0$. These equations can be scaled in the usual way to obtain dimensionless equations for velocity and pressure,

$$\nabla \cdot \mathbf{u} = 0 , \quad (2)$$

$$\nabla p = -\mu\mathbf{u} - \mathbf{n}\delta(\mathbf{x} - \mathbf{x}_t) \cdot \frac{1}{R(s)} \frac{\sigma b^2}{12\mu_2 u_0 L^2} . \quad (3)$$

As dimensionless parameters we have the modified capillary number,

$$\mathrm{Ca} = (12\mu_2 u_0/\sigma)(L^2/b^2) ,$$

characterizing the ratio of viscous forces to surface tension forces and

$$R_\mu = \mu_1/\mu_2$$

denoting the ratio of fluid viscosities. In Eq. (3), μ is a dimensionless viscosity that takes the value 1 in the displaced phase and R_μ in the displacing phase.

B. Vorticity–streamfunction formulation

As a next step, we will rewrite the governing equations in terms of the vorticity and the streamfunction variables. In
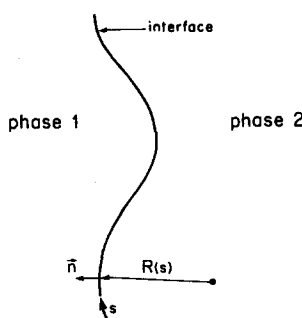

FIG. 1. The interface in the immiscible displacement process is characterized by its arclength parameter s, the local radius of curvature $R(s)$, the unit outer normal vector $\mathbf{n}$, and the unit tangent vector $\mathbf{t}$.

this way, we motivate the use of vortex methods similar to certain ones known from the field of inviscid flows (for a review, see Leonard[23]). We introduce the vorticity ω,

$$\omega = \frac{\partial v}{\partial x} - \frac{\partial u}{\partial y},$$

and the streamfunction ψ,

$$\nabla\psi = (-v, u).$$

Upon taking the curl of the momentum equation (3), and applying the chain rule, we obtain

$$\mu\omega = \nabla\mu \cdot \nabla\psi - \frac{1}{\text{Ca}}\delta(\mathbf{x} - \mathbf{x}_t(s)) \cdot \frac{\partial}{\partial s}\left(\frac{1}{R(s)}\right). \quad (4)$$

Knowing the vorticity distribution, we can reconstruct the velocity field using the Biot–Savart law,

$$\mathbf{u}(\mathbf{x},t) = -\frac{1}{2\pi}\int \frac{(\mathbf{x} - \mathbf{x}') \times \mathbf{e}_z \cdot \omega}{|\mathbf{x} - \mathbf{x}'|^2}\, d\mathbf{x}' + \mathbf{u}_{\text{pot}}(\mathbf{x},t), \quad (5)$$

where $\mathbf{u}_{\text{pot}}(\mathbf{x},t)$ is the potential part of the velocity field.

The momentum equation in its vorticity form (4) presents the key to the numerical simulation, since it states that the flow field contains vorticity only at locations where the mobility varies and where surface tension acts. For an immiscible flow in which the two phases are separated by a sharp interface, the flow field therefore becomes irrotational except for the interface itself, which now corresponds to a vortex sheet of strength $\gamma(s)$. If we neglect the viscosity of the displacing fluid, i.e., if $R_\mu = 0$, we obtain from (4)

$$\gamma(s) = 2\mathbf{u}\cdot\mathbf{t} - \frac{2}{\text{Ca}}\delta(\mathbf{x} - \mathbf{x}_t(s)) \cdot \frac{\partial}{\partial s}\left(\frac{1}{R(s)}\right). \quad (6)$$

Equation (4) furthermore has the advantage of being an algebraic equation, indicating that local information about the flow suffices for the determination of the value of the vorticity.

III. NUMERICAL TECHNIQUE

A. Computational procedure

In the following, we describe our numerical technique for the simulation of two-dimensional immiscible Hele-Shaw flows. It is based on Eqs. (5) and (6) and it tracks the vortex sheet at the interface in a purely Lagrangian reference frame. We assume the flow to be periodic in the spanwise y direction and to extend to infinity in the streamwise x direction.

The use of periodic spanwise boundary conditions allows certain efficiencies in the numerical procedure, but one may naturally question the relevance to experiments in which a no-flux condition is appropriate. In the case of symmetric steady fingers that propagate without change of form, the two conditions are equivalent; for unstable fingers that undergo asymmetrical tip splitting (to be discussed below) they are not. Thus comparison between our results and those from experiments must be made with caution. However, as it will develop below, most of the observed phenomena are associated with the local behavior at the tip, and are not likely to be substantially different for the two sets of boundary conditions. In any event, we believe that most of our conclusions regarding the mechanisms of tip splitting are

robust and independent of side-wall boundary conditions.

For choosing the optimum way of discretizing the vortex sheet, it is important to notice that the only physical length scale in the problem is set by the surface tension. It has the effect of damping small scales that otherwise would exhibit linear growth rates inversely proportional to their wavelength. Consequently, for a study of the physically interesting limit of low surface tension, i.e., high capillary number, extreme care has to be taken in the process of discretizing the vorticity field. The goal is to minimize the effect of introducing a numerical length scale through the discretization procedure. In the current work, we gain a smooth and accurate representation of the vorticity sheet by discretizing it into n circular arcs as shown in Fig. 2. Mangler and Smith[24] were the first ones to represent a vortex sheet by a single circular arc. The continuous distribution of the vortex sheet strength along arc i is assumed to be of the form

$$\gamma_i(\phi) = \alpha_i + \beta_i \sin\phi.$$

Mangler and Smith showed that this distribution has the advantage that the velocity field associated with it can be obtained by integrating the Biot–Savart law analytically. Here α_i is the average vortex sheet strength of the two end points of the circular arc and β_i provides a continuous transition along the arc between these endvalues. Recently, this form of discretization has been successfully employed by Higdon and Pozrikidis[25] in their investigation of the evolution of a vortex sheet in inviscid flow.

After setting an initial interface shape, the calculation proceeds in discrete time steps as follows. At every time step, the velocities of n marker points $\mathbf{x}_i$ (one per circular arc) on the interface are determined by integrating over the vorticity distribution of all other circular arcs using the Biot–Savart law. An analytical expression taking into account the periodic images of the interface in the spanwise y direction can be derived by analytical summation (Higdon and Pozrikidis[25]). We evaluate this integral by using a trapezoidal finite
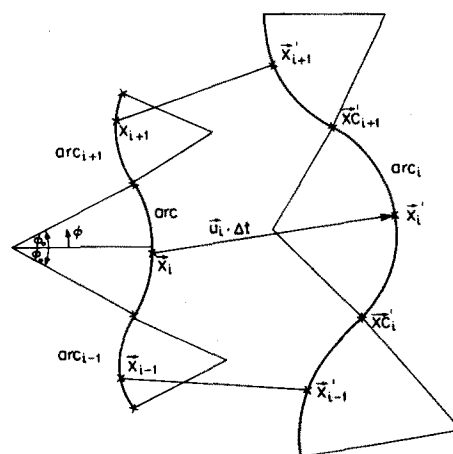

FIG. 2. The interface is discretized into circular arcs. Each arc is represented by a marker point x, which is advanced over a time step Δt. Subsequently, the end points xc of the new circular arcs at the updated time level are found as the centers between the x on a spline representation of the interface based on all marker points.

difference scheme, which is sufficient since the overall error in evaluating the velocity of x_i is determined by the accuracy of the integration over the interfacial section next to x_i. For the same reason, the velocity induced on a marker particle by a vortex sheet arc is evaluated by means of the point vortex approximation if the distance between arc and marker particle exceeds the width of the Hele–Shaw cell.

Once the velocities of the marker particles are known, these are advanced over the time step by a fourth order Runge–Kutta method. As a result, we have the position of the interface at the new time at n discrete points x_i'. We now fit a new set of n circular arcs through these points in the following way. First a cubic spline is fitted through the updated x_i', with the straight-line distance between the points serving as the splining parameter. This spline representation then allows us to find the midpoints xc_i' between the x_i'. Subsequently, a new circular arc is fitted through each set xc_i', x_i', xc_{i+1}'.

As a next step, the vorticity distribution has to be updated. For this purpose, we first determine the values of the vortex sheet strength at the x_i' using Eq. (6). As an initial estimate, $\nabla\psi$ is approximated by the velocity values of the previous time step. By applying a cubic spline we find the vortex sheet strength at xc_i' and xc_{i+1}', upon which the coefficients α_i' and β_i' can be determined in the way described above. An iterative procedure is subsequently applied until the new values of the velocities have converged.

At fixed time intervals, the marker points x_i along the interface are redistributed and new ones are added in order to avoid deteriorating resolution as a result of local interface generation. This remeshing procedure takes into account the local capillary number at $x = x_t(s)$ formed with the local velocity component $u(x_t(s)) \cdot n(x_t(s))$ normal to the interface,

$$ \mathrm{Ca}(x_t(s)) = \frac{12\mu_2 u(x_t(s)) \cdot n(x_t(s))}{\sigma} \cdot \frac{L^2}{b^2}, $$

and requires that even the shortest wavelength with a positive linear growth rate for this capillary number,

$$ l_c = 2\pi/\mathrm{Ca}^{1/2}, $$

is resolved by a certain number of points, typically four or eight. In order to provide adequate resolution, the spacing Δs between the marker points in addition is reduced in regions of high interface curvature by requiring

$$ \Delta s + c/R(s) $$

instead of Δs to be less than this fraction of l_c, where c is a constant. Similar remeshing criteria were employed by De-Gregoria and Schwartz[20] in their boundary integral technique.

As the initial interface becomes more and more convoluted, the rate of change of the flow variables increases rapidly, so that the time step has to be reduced. It is adjusted in such a manner that the difference between the final corrector velocity and the initial predictor velocity, multiplied by the actual time step, nowhere in the flow exceeds a certain numerical value established in test calculations. Acceleration effects are most pronounced in the "active" sections of the interface, i.e., the fingertips. Those sections left behind in the

displacement process, on the other hand, move at small and almost constant velocities. Our numerical algorithm takes advantage of this fact by employing a local time-stepping procedure that updates the velocities of the most active interface sections more often than those of the rest of the interface. This results in significant savings, especially in the advanced stages of finger growth, since a large fraction of the interface becomes passive.

In order to simulate slight imperfections present in every experimental Hele–Shaw apparatus, we superimpose small random perturbations of the following form on the motion of the marker particles: at every step, u and v perturbations are added to the velocity components evaluated from the Biot–Savart law. They are assumed to be proportional to the velocity components themselves, to a random number with a uniform distribution between -1 and 1, and, to a constant representing the amplitude of the random noise.

In summary, we apply a numerical procedure that achieves high spatial accuracy while minimizing the effect of setting a numerical length scale by discretizing the vorticity sheet along the interface into circular arcs with a continuous vorticity distribution. The method is of fourth order in time and partly compensates the $O(N^2)$ operation count associated with the direct interaction algorithm by using a locally refined discretization as well as local time stepping. All calculations were carried out on the CRAY X-MP of the San Diego Supercomputer Center.

B. Validation of the numerical algorithm

In the following, we compare numerical results for immiscible flows obtained with our algorithm with analytical and numerical results of other authors in order to validate our numerical procedure and investigate its limitations. The calculations presented in this section typically required less than one minute of CPU time.

1. Flows with vanishing surface tension

Aitchison and Howison[26] report analytical results for the evolution of the interface in a linear Hele–Shaw cell of width 2π in the case of vanishing surface tension. They find that if at $t = 0$ the boundary between the two fluid phases consists of a slightly perturbed planar interface of the shape

$$ x = \epsilon \cos \varphi, \quad y = \varphi - \epsilon \sin \varphi, \quad 0 \leqslant \varphi \leqslant 2\pi, $$

the perturbation will grow until, at a time

$$ t_{\mathrm{crit}} = \frac{1}{u_0}\left[\frac{\epsilon^2}{2} - \frac{1}{2} + \ln\left(\frac{1}{\epsilon}\right) \right], $$

a cusp will form. Here u_0 is the velocity at which fluid is injected into the cell. For this flow there exists no natural length scale, which makes its simulation a difficult test case for the validation of our numerical method. Since the problem does not involve a damping mechanism, any computational technique that does not introduce some numerical damping will break down after a finite time $t < t_{\mathrm{crit}}$ as a result of the fact that discretization and roundoff errors trigger the growth of short wavelength oscillations (for an example of this with finite difference methods, see Aitchison and Howison[26]). Consequently, the time up to which a numerical
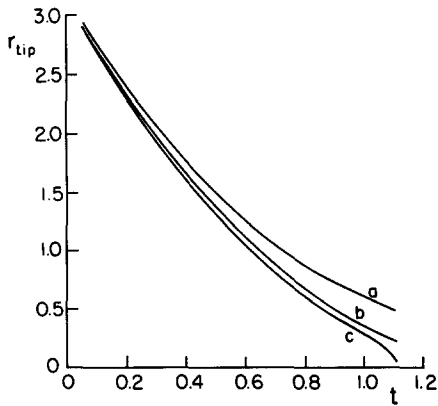
FIG. 3. The numerical simulation of the flow without surface tension analyzed by Aitchison and Howison.[26] Shown is the temporal decrease of the minimum radius of curvature r_{tip} along the interface for various discretizations. a: Initial discretization of the interface into nine segments; b: initial discretization of the interface into 15 segments; c: initial discretization of the interface into 19 segments. The analytical solution predicts the appearance of a cusp singularity at time $t_{crit} \approx 1.129$.

scheme without artificial damping is able to yield a smooth solution for different levels of discretization presents an indication of the numerical stability characteristics of the computational algorithm. We have attempted to study the evolution of the interface for the case $\epsilon = 0.2$ and $u_0 = 1$ in which the cusp should appear at $t \approx 1.129$. Figure 3 shows the minimum radius of curvature of the interface as a function of time for successively finer discretizations of the interface. The number of marker points given in Fig. 3 indicates the initial number; remeshing took place after time intervals of 0.05.

As the resolution of the vortex sheet is refined and the time step is reduced, the correct time for the formation of the cusp is approached, thus demonstrating convergence of our numerical scheme. Figure 4 shows the evolution of the interface with time, and the emerging singularity at the tip is clearly visible. The numerical algorithm is able to follow the decrease of the radius of curvature at the tip over more than an order of magnitude, well into a regime where the interface exhibits a small region of very high curvature. This test cal-
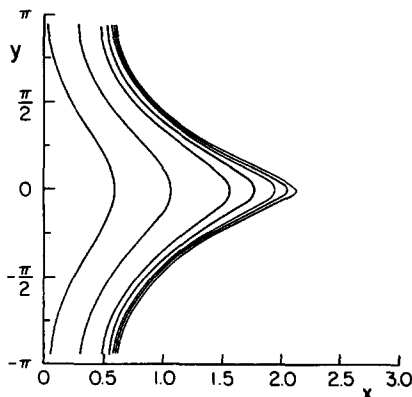
culation demonstrates the ability of the numerical scheme to correctly track a variety of length scales. Numerical instability effects do not noticeably influence the solution until very late in time, when the minimum radius of curvature has become very small.

2. Steady fingers with surface tension

Finite values of surface tension introduce a physical length scale into the problem. They damp short waves and prevent the evolution of a singularity in the interface shape and steady finger shapes are possible. McLean and Saffman[27] calculated the width of steady Hele–Shaw fingers as a function of the capillary number. These numerical solutions to the steady equations are generally accepted as being correct and highly accurate. They have been used by other authors (Tryggvason and Aref,[28] DeGregoria and Schwartz[20]) to validate their time-dependent numerical procedures. Figure 5 compares our numerically obtained results for the finger width with those of McLean and Saffman. (For clarity, we present our results in the same form as Tryggvason and Aref[28] and DeGregoria and Schwartz[20].) We have carried out two sets of calculations in which the shortest wavelength unstable under local conditions is discretized into four or eight segments, respectively. Since this wavelength decreases as the capillary number is increased, the number of computational elements grows continually in each of the two sets of simulations as the surface tension is reduced. Our numerical results approach the ones by McLean and Saffman[27] as the discretization is improved. For the finer discretization they reproduce their results with high accuracy for the whole range of capillary numbers investigated (from about 10 to 330).

IV. RESULTS

In order to investigate the range of capillary numbers where the transition from steadily advancing fingers to unstable ones occurs, we have carried out a first simulation for $Ca = 530$. This corresponds to a value of dimensionless sur-

FIG. 4. The evolution of the interface in time. The cusp is forming at the tip of the interface.
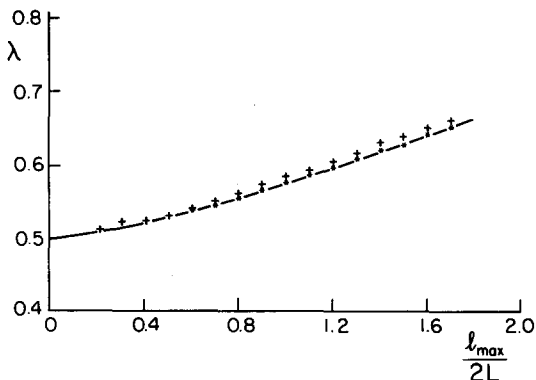

FIG. 5. Comparison of the numerically obtained ratio of finger width to cell width as a function of the dimensionless surface tension with the exact solution by McLean and Saffman.[27] + : Discretization into four segments per shortest wavelength linearly unstable under local conditions; *: discretization into eight segments per shortest wavelength linearly unstable under local conditions; -: McLean–Saffman solution.

face tension *in between* the solution tracks observed by De-Gregoria and Schwartz[21] ($\tau = 0.000\,47$ in their notation). The simulations reported by these authors do not result in a steady-state finger at this capillary number, and instead a tip-splitting instability occurs. Our computation employs a version of our code that assumes symmetry about the channel centerline. Like all the simulations reported in this section, it discretizes the shortest wavelength unstable under local conditions into four segments. It starts from a flat interface with a sinusoidal displacement of amplitude 0.064 and wavelength equal to the width of the cell. The time step is 2.8×10^{-4} throughout the simulation, with remeshing occurring every six time steps. We do not superimpose random perturbations in the course of the simulation. Figure 6 shows the evolution of the interface at different time levels, along with a plot of the marker particle positions at the final time. The impression of a steadily advancing finger gained from this graph is confirmed by Fig. 7, which shows the evolution of the tip velocity and tip radius of curvature as a function of the tip location. We recognize that both quantities, after an initial transient evolution, display only very small fluctuations, so that we can regard the finger as steadily advancing. It should be kept in mind that the flow is unsteady in a fixed frame since the interfacial length grows continuously although the fingertip advances in a steady fashion. This requires frequent remeshing and the addition of new marker points. As a result, small fluctuations always have to be expected. We note that the average value of the tip velocity u_{tip} is about 1.967 and clearly remains below 2, which means that the effective ratio of finger width to cell width,

$$\lambda_{\text{eff}} = 1/u_{\text{tip}} ,$$

is about 0.507. This point is also plotted in Fig. 5, thus indicating the high accuracy of our results.

For Ca = 833 we obtain a different result. This capillary number represents the value of dimensionless surface tension at which DeGregoria and Schwartz[21] observe a quasi-steady-state finger of about 0.471 times the cell width ($\tau = 0.000\,30$ in their notation). As before, we apply the symmetric version of our code without superimposing noise. While our interface configurations at different time levels (Fig. 8) initially also seem to indicate a steadily advancing finger, graphs of the tip velocity and the tip radius of curvature (Fig. 9) show that these quantities never settle down to a nearly constant value. Instead, their fluctuations grow until finally a tip-splitting event occurs. By the time this event
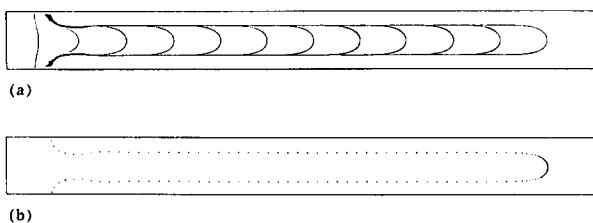

FIG. 7. Ca = 530. (a) The velocity of the fingertip as a function of the fingertip location. After an initial transient period the tip velocity displays only small fluctuations around an average value of approximately 1.967. This indicates an average finger width of about 0.507 times the cell width. (b) The radius of curvature at the fingertip as a function of the fingertip location. It also exhibits only small fluctuations, indicating the existence of an almost steady finger at this capillary number.

becomes detectable in the plot displaying the interface, the finger has advanced over a distance nearly fifteen times its width, suggesting that one has to be careful interpreting results of initial value calculations as representing steady solutions. Furthermore, Fig. 9(a) shows that the average value of the tip velocity u_{tip} remains clearly below 2 even for this unsteady evolution, so that again the effective finger width is above half the cell width. A Fourier transformation of the function depicted in Fig. 9(a) does not show a clear domination of one or more frequencies, indicating that the evolution of the instability cannot simply be described as the growth of oscillations of a constant period.

As we increase the capillary number further, the instability sets in more rapidly. As a next step, we investigate the flow at Ca = 1111, which corresponds to the lowest value of the dimensionless surface tension studied by DeGregoria and Schwartz[20] ($\tau = 0.000\,225$ in their notation). We now allow general, asymmetric solutions. As before, we start the simulation by giving the initially flat interface a sinusoidal

FIG. 6. Ca = 530. (a) Evolution of the interface in time. (b) Discretization of the interface at the final time of the simulation. The discretization is finest at the fingertip, since both the local capillary number and the curvature are large there.
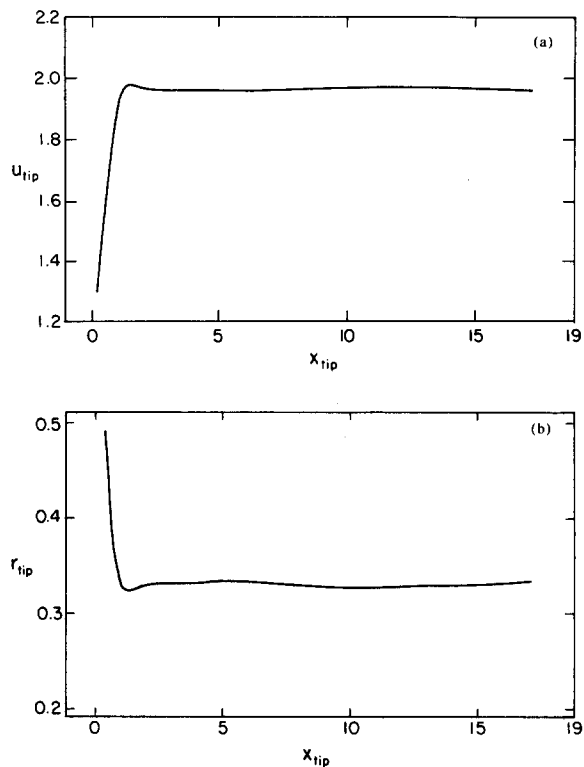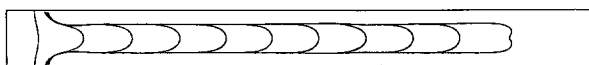

FIG. 8. Ca = 833. While the evolution of the interface initially seems to proceed towards a steady state, it eventually develops a tip-splitting instability.
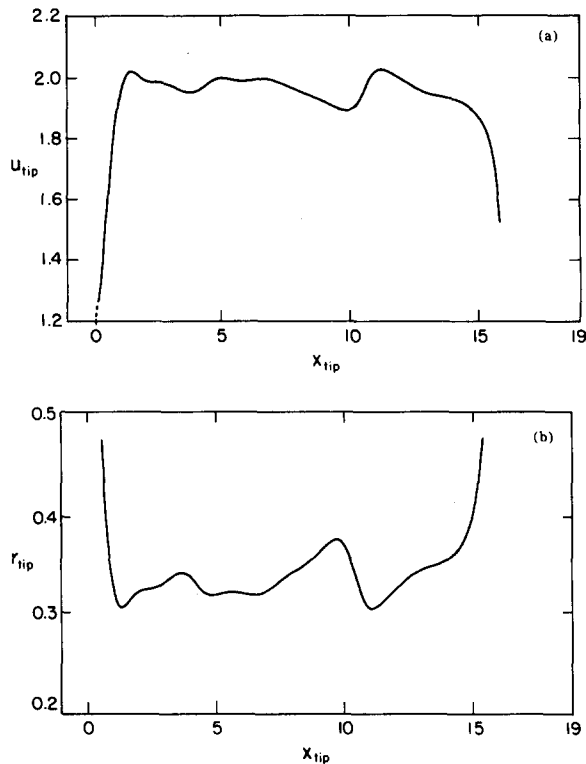
FIG. 10. Ca = 1111. All fingers grow in an unstable fashion through a series of tip-splitting events. The degree of asymmetry determines how fast the larger lobe emerging from the splitting process outgrows the smaller one. (a) Case I: Superimposed on the velocity components obtained from the Biot–Savart law are random fluctuations of amplitude 3.2×10^{-4}. Times are 0.10, 0.48, 1.08, 1.72, 2.36, 3.00, 3.62, 4.26, 4.90, 5.54, and 6.18. (b) Case II: Here the fluctuations have an amplitude of 1.6×10^{-3}. Times are 0.10, 0.76, 1.40, 2.04, 2.68, 3.32, 3.94, and 4.58. (c) Experimentally observed finger at Ca = 2200 (Kopf-Sill and Homsy[9]).

FIG. 9. Ca = 833. (a) The tip velocity as a function of the tip location. After the initial transient phase the tip velocity develops oscillations that grow in amplitude and eventually lead to a tip-splitting event. (b) The tip radius of curvature as a function of the tip location. It develops oscillations almost in antiphase to the oscillations of the tip velocity.

displacement of amplitude 0.064 and wavelength equal to the width of the Hele–Shaw cell. In order to study the effect of the random fluctuations, two simulations were carried out for Ca = 1111 with different amplitudes. In case I it had the value of 3.2×10^{-4}, whereas for case II it was 1.6×10^{-3}.

The resulting finger shapes for the two cases are depicted in Fig. 10 for various times. We see that in both cases the fingers grow through a series of spreading, splitting, and shielding events: after the finger has reached a certain critical width, which for Ca = 1111 is approximately half the cell width, it splits into two lobes. If this splitting occurs in a nearly symmetrical fashion, the two emerging lobes grow side by side for a relatively long time, see, for example, the second splitting in case II. Eventually, however, through a shielding process, the slightly more advanced finger outgrows its competitor. While it continues to spread and to proceed towards the next splitting, the outgrown finger stops advancing altogether. The more asymmetrical the splitting, the more quickly one of the two lobes wins the competition. We can also recognize how, after the smaller lobe has practically stopped advancing, its development is dominated by surface tension forces, which try to smooth out regions of high interface curvature. Figure 10(c) depicts an experimentally observed finger for Ca = 2200 (Kopf-Sill and Homsy[9]). Despite the difference in capillary numbers, we observe the same qualitative features as in the numerical simulation.

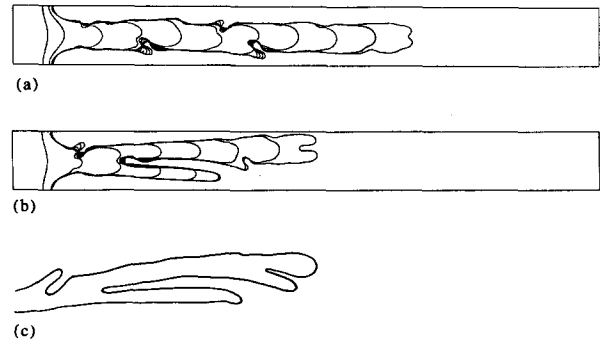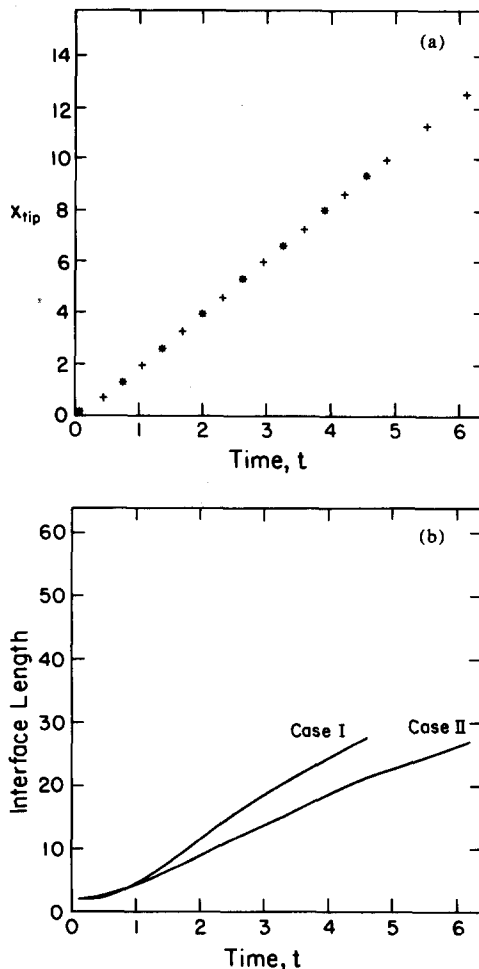In Fig. 11 we have plotted the fingertip location and the

FIG. 11. Solution properties. (a) The tip locations as functions of time for the two simulations at Ca = 1111. The calculation shown in Fig. 10(a) is denoted by +, while * represents the finger of Fig. 10(b). Both fingers advance at approximately the same average velocity, indicating that for the range investigated the amplitude of the random fluctuations has a negligible effect on the finger width. (b) The interfacial lengths as functions of time for the two simulations shown in Figs. 10(a) and 10(b). Because of the almost symmetric second splitting event, case II exhibits a faster growth in interfacial arclength.
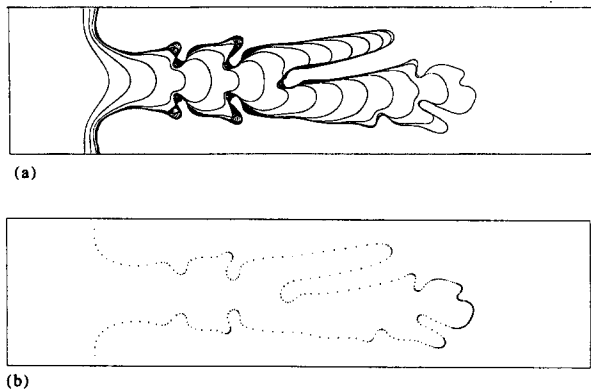
(a)

(b)

FIG. 12. Ca = 2500. (a) The evolution of the interface with time. Times are 0.0, 0.16, 0.32, 0.48, 0.64, 0.80, 0.96, 1.12, 1.28, 1.44, 1.60, 1.74, 1.90, 2.06, and 2.22. (b) At the final time of the simulation, the interface is discretized into 407 circular arcs. A qualitative difference as compared to the fingers shown in Fig. 10 is the appearance of the three-lobe splitting process. Splitting events are more frequent at this capillary number than at Ca = 1111, indicating a decrease in the characteristic length.

FIG. 13. Ca = 2500. Tip location as function of time. The nearly constant average tip velocity is approximately 2.3, indicating an effective finger width of about 0.435 times the cell width.

total interfacial length as a function of time for both cases. We see that the average tip velocity is almost identical for the two simulations, indicating that the amplitude of the random fluctuations has little influence on the effective average finger width. The average tip velocity evaluated from Fig. 11(a) is about 2.08, so that the effective finger width is 0.480. As expected, different random perturbations can very well affect the degree of symmetry of each individual splitting process. This is reflected by the graph depicting the interfacial length as a function of time, which shows a more rapid increase for case II during the time of the side-by-side growth of the two lobes.

In order to study how the features of the emerging fingers change as surface tension forces diminish, we have carried out a simulation for Ca = 2500, with the corresponding finger shape depicted in Fig. 12. Several factors render this calculation considerably more costly (CPU time on a CRAY X-MP was approximately 15 hours) than the previously described one. First of all, the lower value of the surface tension requires a finer discretization, which enters the operation count quadratically because of the direct interaction nature of the algorithm. It furthermore results in more frequent splitting events, thus causing the interfacial length to grow more rapidly. In addition, the finer discretization leads to a more stringent condition for the allowed time step, which for the Ca = 2500 simulation was 3.2×10^{-5} after an initial transient phase. As a consequence, it is about an order of magnitude more expensive for the Ca = 2500 calculation to reach a certain time level than for the Ca = 1111 case. As for the lower Ca cases, we started the simulation from an interface with a sinusoidal displacement, this time of amplitude 0.32. Random perturbations of amplitude 3.2×10^{-4} were then superimposed at each time step. We see in Fig. 12(a) that the initial phases of the evolution of the finger are dominated by the symmetry of the initial perturbation. Only after the third splitting does the asymmetry of the random perturbations become clearly visible. The right finger outgrows the left one and advances through a
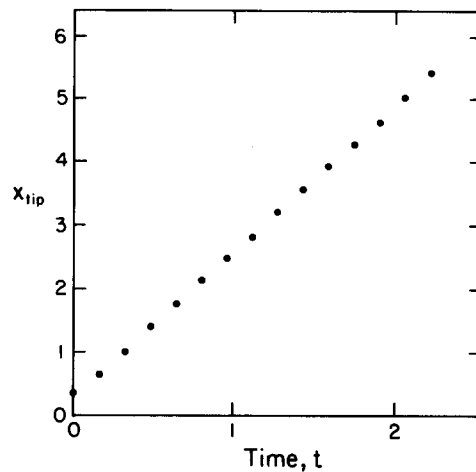
series of splitting events. Figure 12(b) shows the discretization into 407 circular arcs at the final time of the simulation. The splitting events now occur more frequently than for Ca = 1111, indicating a decrease in the characteristic length scale of the flow. This is also obvious from the fact that the finger splits before it has widened to half the cell width. Furthermore, the decrease of the effective finger width is reflected in the plot of the tip location as a function of time (Fig. 13). This graph indicates that the fingertip moves at an almost constant average velocity of about 2.3, corresponding to an effective finger width of 0.435. However, we recognize from Fig. 14, which depicts the tip velocity, i.e., the velocity of the point with the largest x coordinate, a function of the tip location, that the tip velocity actually varies throughout the evolution of the finger. It decreases during the phase in which the finger spreads, while it increases during the splitting process. After the initial transient phase, the interfacial length grows approximately linearly in time (Fig. 15). However, as a consequence of the increased splitting frequency, the growth rate is clearly higher for Ca = 2500 than for Ca = 1111.

An interesting aspect distinguishing the Ca = 2500 case from the Ca = 1111 simulations is related to the nature of the observed splitting events. While in the former the fingers grow through a series of two-lobe splittings, the latter exhib-
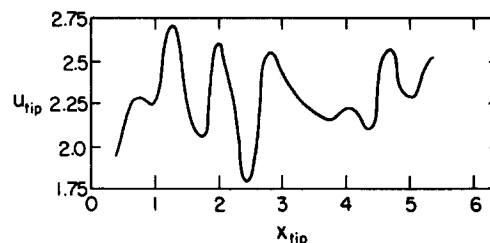

FIG. 14. Ca = 2500. Tip velocity as a function of tip location. Although the average tip velocity is nearly constant, we see strong fluctuations in the instantaneous values. While the tip velocity increases during a splitting event, it decreases while the finger is spreading.
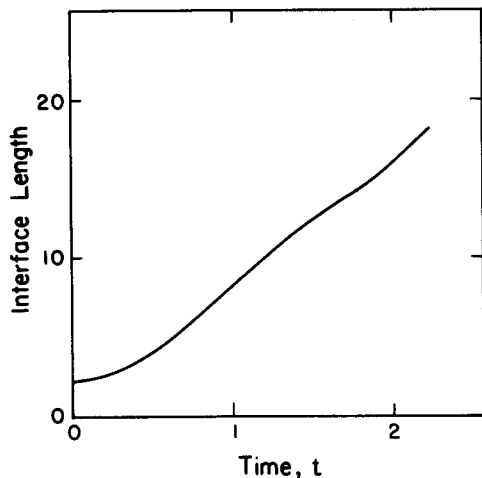
FIG. 15. Ca = 2500. Growth of the interfacial length as a function of time. As a consequence of the more frequent splitting events, the interface grows at a much faster rate than for Ca = 1111.

its a new type of splitting event resulting in the generation of three new lobes instead of two. Both the first two splittings and the next to last one display this feature. This observation is intriguing insofar as the tip of the finger evolves oppositely in the two types of splittings. While in the two-lobe splitting it slows down and eventually stops growing altogether, it accelerates in the three-lobe splitting, outgrows the two side lobes, and remains the most advanced part of the finger.

In order to answer the question as to what decides in which way the finger instability proceeds, we return to the symmetric simulation for Ca = 833 described earlier in this section. From the graphs depicting the tip velocity and the tip radius of curvature as a function of the tip location [Figs. 9(a) and 9(b)], we recognize that the finger instability evolves in an oscillatory fashion. The oscillations of the tip velocity and the tip radius are almost in antiphase, i.e., the tip radius reaches a maximum when the tip velocity is at its minimum value. We can see that these oscillations grow in their amplitudes until they eventually escape from their oscillatory trajectories, thus indicating that a splitting event is happening. This oscillatory evolution of the tip-splitting instability explains why we sometimes observe a two-lobe splitting and sometimes a three-lobe splitting. If the trajectory of the tip velocity escapes from its oscillatory behavior on a downswing and the tip radius on an upswing, then the tip will slow down during the splitting event, thus leading to the emergence of two new lobes. If, on the other hand, the tip velocity leaves the oscillatory trajectory on an upswing with the tip radius being on a downswing, then the tip accelerates and outgrows the two side lobes, with the result of three new lobes emerging.

The preceding analysis shows that the finger instability evolves via an oscillation of the fingertip. This indicates the crucial role of the fingertip in the course of the evolving instability. Experimental investigations referred to in the Introduction (Couder et al.[10,11]) demonstrate that the nature of the finger instability changes dramatically if the region close to the fingertip is perturbed, for example, by introducing a bubble into the experiment. This becomes understanda-

ble in the light of the above analysis. Since in the experiment the bubble placed at the fingertip forces the tip radius to stay more or less constant, it is obvious that this quantity cannot develop a growing oscillation with the eventual escaping event. In order to study the behavior of a finger when the tip is artificially influenced, we carried out a set of numerical simulations in which we held the tip radius constant over a small region close to the fingertip.

For Ca = 1111, we started the simulation with a fully developed finger, the tip of which is initially located at $x = 6$. As the initial ratio of finger width to cell width we take the value of 0.5, which is close to the effective finger width obtained in the previous unforced Ca = 1111 calculations. The initial shape of the fingertip corresponds to the Saffman–Taylor solution for this finger width. From the very start we hold the tip curvature constant between $y = -0.2$ and $y = 0.2$, while we superimpose random perturbations of amplitude 1.6×10^{-3} as in the unforced case II. As we can see in Fig. 16, the finger now proceeds in a steady fashion (as opposed to the unforced flow at the same Ca number, which was unstable), without showing any signs of a splitting instability. This indicates the stabilization resulting from a perturbation that prevents the tip radius from oscillating.

In all our simulations, we have never observed any steady fingers with $\lambda < 0.5$ in the unforced flow. In order to investigate whether or not forcing would allow for such fingers, we have carried out a symmetric simulation without random perturbations for Ca = 500 in which we started from a fully developed finger of width ratio 0.35. We hold the tip radius constant between $y = -0.032$ and $y = 0.032$. The fingertip initially is at $x = 6.4$, and the initial tip shape is identical to the Saffman–Taylor solution for this width. We do not superimpose random perturbations. As we see in Fig. 17(a), the narrow finger now proceeds in a steady fashion, without showing any signs of widening or splitting. If we do not hold the tip curvature constant, the finger starts to widen immediately [see Fig. 17(b)].

If we raise the Ca number to 2500, we observe that the finger now goes unstable with respect to a different instability mode, if we hold the tip radius constant between $y = -0.064$ and $y = 0.064$ (Fig. 18). The fixed radius of curvature at the tip prevents it from becoming unstable with respect to the tip-splitting instability, and instead a dendritic instability develops with the resulting lobes branching out sidewards. These dendrites evolve from oscillations of the interface close to but outside the region in which the curvature is held constant.

V. DISCUSSION

We have presented numerical simulations of the evolution of viscous fingers in immiscible Hele–Shaw flows. The

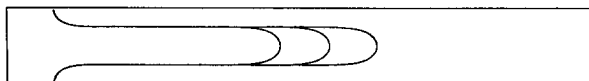

FIG. 16. Ca = 1111. By holding the tip radius constant between $y = -0.2$ and $y = 0.2$, we are able to stabilize the finger, which without this forcing developed as shown in Fig. 10(b).
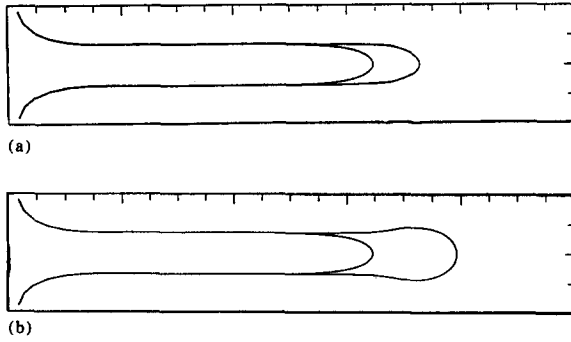
(a)

(b)

FIG. 17. Ca = 500. (a) Holding the tip curvature constant between $y = -0.032$ and $y = 0.032$ allows for the evolution of a steady finger of width 0.35 times the cell width. (b) Without forcing, the finger immediately starts to widen.
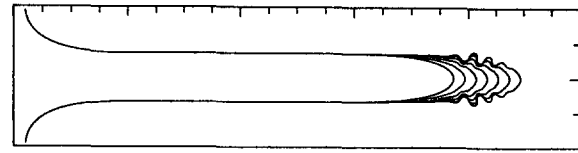

FIG. 18. Ca = 2500. Holding the tip radius constant between $y = -0.064$ and $y = 0.064$ results in a dendritic instability of the finger similar to the one observed by Couder et al.[11]

discretization of the vortex sheet at the interface into circular arcs with a continuous distribution of circulation, along with the analytic integration via the Biot–Savart law, offer the potential of higher accuracy than the previously used numerical schemes. Test calculations for the evolution of a cusp in a flow without surface tension as well as for the width of steady fingers as a function of the dimensionless surface tension, demonstrate the high accuracy that can be obtained with the present scheme. Over the full range of capillary numbers investigated, which extends from approximately 10 to 330 for the test calculations, our results for the width of steady fingers agree well with the solutions obtained by McLean and Saffman.[27] Without some kind of artificial forcing, we never observe steady fingers of width less than one-half the cell width, and thus we do not confirm the narrow finger solutions reported by DeGregoria and Schwartz.[21] They report, for example, a quasi-steady-state finger of $\lambda \approx 0.471$ for Ca = 833 ($\tau = 0.000\,30$ in their notation). However, their calculation is terminated at time $t = 4$. Our calculations, on the other hand, show that after a long time ($t \approx 8$) the finger develops a tip-splitting instability at this capillary number. Up to the time at which the tip-splitting process occurs, the average tip velocity is less than 2, which means the effective ratio of finger width to cell width is larger than one-half. We also do not find any indications of multiple solution tracks as reported by DeGregoria and Schwartz[21] (1987). While they do not obtain a steady finger at Ca = 530($\tau = 0.000\,47$ in their notation), which according to their results is a value in between two tracks of stable solutions, we observe a finger that exhibits only very small fluctuations in the tip velocity and that does not seem to proceed towards a splitting event. It has an average λ of about 0.507, and thus it appears to be in good agreement with the solutions of McLean and Saffman.[27]

Our numerical simulations for Ca = 1111, on the other hand, agree with the results presented by DeGregoria and Schwartz[20] in that they show the finger to be unstable. We observe a ratio of effective finger width to cell width of about 0.480 for the two cases of different random perturbations. Experimental observations by Kopf-Sill and Homsy[9] for Ca = 1180 show an effective ratio of finger width to cell width of about 0.40. One of the reasons for this discrepancy

might be found in stronger perturbations affecting the experimental finger and causing it to split before it reaches the same critical width as in the simulation. In addition, at this value of Ca, three-dimensional effects are likely to be of some importance in the experiments. Furthermore, the calculations assume periodic boundary conditions in the spanwise direction, whereas in the experiment, the side walls establish a no-flux condition. After the initial transient phase, the growth rate of interfacial length with time is 4.5 for case I and 6.5 for case II (a steady finger advancing with velocity 2 would have a growth rate of 4). The experiment, on the other hand, shows a growth rate of 10, which is consistent with the smaller effective finger width.

We have subsequently extended our simulations to Ca = 2500, which requires about an order of magnitude more computational work than the simulations for Ca = 1111. Several features of the numerical results demonstrate the decrease of the characteristic length scale as compared to Ca = 1111. The effective finger width drops to 0.435, and the splitting frequency increases significantly. This is reflected in a comparison of the growth of arclength over time for the two capillary numbers [Figs. 11(b) and 15]. The much higher growth rate of 8.0 for Ca = 2500 indicates the generation of smaller scales on the interface, since the area of the finger is proportional to the elapsed time. The experiments by Kopf-Sill and Homsy show a growth rate of 11.2 for Ca = 1900 and 14.0 for Ca = 3211, which again is higher than in the simulation.

A qualitative difference between the simulations for Ca = 1111 and Ca = 2500 is the appearance of three-lobe splitting events at the higher value of the capillary number. This result is in agreement with experimental observations by Kopf-Sill and Homsy, who find that three-lobe splittings gain importance at higher Ca. The possibility of numerically monitoring the tip velocity as well as the radius of curvature at the tip enables us to identify the two-lobe and the three-lobe splitting as different manifestations of the same mechanism, namely, an oscillatory evolution of the tip instability. Depending on whether the tip curvature and the tip velocity exceed threshold values on an upswing or on a downswing, the result will be either a two-lobe or a three-lobe splitting. It appears that at higher capillary numbers it becomes more likely for the tip oscillation to develop into a three-lobe splitting. The tip-splitting instability of viscous fingers might thus be similar in its evolution to the instability exhibited by a large spherical gap bubble in inviscid flow and other related problems of the stability of curved fronts (Pelce and Clavin[29] and Batchelor[30]).

The analysis of the crucial role the tip plays in the evolu-

tion of the splitting instability makes it immediately understandable why fingers with an artificial constraint that prevents the tip from developing the oscillatory behavior do not exhibit the splitting instability (Couder et al.[10,11]). Instead they remain stable up to considerably higher capillary numbers at which they develop a dendritic instability. From this argument it appears that the dendritic instability is a natural instability mode that is present even in the unforced flow. However, it is normally not observed since the splitting instability sets in first. We could numerically demonstrate the stabilization of the finger against the tip-splitting instability and the onset of the dendritic instability at higher capillary numbers by holding the tip radius of curvature constant in a small region close to the tip. Furthermore, we could show how the forcing can allow for steady fingers to develop with a width of considerably less than half the cell width. This observation could lend support to the hypothesis of Hong and Langer,[16] who show that in order for a steady unforced finger to develop with $\lambda < 0.5$, an apparent cusp at the fingertip has to be present. The constraint on the curvature at the fingertip in the experiment and in the simulations could then have the same effect on the finger width as a cusp at the tip. However, we cannot provide an explanation for the experimental observation by Kopf-Sill and Homsy[12] of narrow fingers without artificial perturbation.

ACKNOWLEDGMENTS

[1]S. Hill, Chem. Eng. Sci. 1, 247 (1952).
[2]R. L. Chuoke, P. van Meurs, and C. van der Poel, Trans. AIME 216, 188 (1959).
[3]P. G. Saffman and G. I. Taylor, Proc. R. Soc. London Ser. A 245, 312 (1958).
[4]R. A. Wooding and H. J. Morel-Seytoux, Annu. Rev. Fluid Mech. 8, 233 (1976).
[5]P. G. Saffman, J. Fluid Mech. 173, 73 (1986).
[6]G. M. Homsy, Annu. Rev. Fluid Mech. 19, 271 (1987).
[7]C.-W. Park and G. M. Homsy, Phys. Fluids 28, 1583 (1985).
[8]T. Maxworthy, J. Fluid Mech. 177, 207 (1987).
[9]A. R. Kopf-Sill and G. M. Homsy, Phys. Fluids 31, 18 (1988).
[10]Y. Couder, N. Gerard, and M. Rabaud, Phys. Rev. A 34, 5175 (1986).
[11]Y. Couder, O. Cardoso, D. Dupuy, P. Tavernier, and W. Thom, Europhys. Lett. 2, 437 (1986).
[12]A. R. Kopf-Sill and G. M. Homsy, Phys. Fluids 30, 2607 (1987).
[13]C.-W. Park and G. M. Homsy, J. Fluid Mech. 139, 291 (1984).
[14]P. Tabeling, G. Zocchi, and A. Libchaber, J. Fluid Mech. 177, 67(1987).
[15]D. Reinelt, Phys. Fluids 30, 2617 (1987).
[16]D. C. Hong and J. S. Langer, submitted to Phys. Rev. A.
[17]R. Combescot, T. Dombre, V. Hakim, and Y. Pomeau, Phys. Rev. Lett. 56, 2036 (1986).
[18]D. C. Hong and J. S. Langer, Phys. Rev. Lett. 56, 2032 (1986).
[19]B. I. Shraiman, Phys. Rev. Lett. 56, 2028 (1986).
[20]A. J. DeGregoria and L. W. Schwartz, J. Fluid Mech. 164, 383 (1986).
[21]A. J. DeGregoria and L. W. Schwartz, Phys. Rev. Lett. 58, 1742 (1987).
[22]E. Meiburg and G. M. Homsy, in Numerical Simulation in Oil Recovery, IMA Volume II, edited by M. Wheeler (Springer, Berlin, 1988), pp. 199–225.
[23]A. Leonard, Annu. Rev. Fluid Mech. 17, 523 (1985).
[24]K. W. Mangler and J. H. B. Smith, Proc. R. Soc. London Ser. A 251, 200 (1959).
[25]J. J. L. Higdon and C. Pozrikidis, J. Fluid Mech. 150, 203 (1985).
[26]J. M. Aitchison and S. D. Howison, J. Comput. Phys. 60, 376 (1985).
[27]J. McLean and P. G. Saffman, J. Fluid Mech. 102, 455 (1981).
[28]G. Tryggvason and H. Aref, J. Fluid Mech. 154, 287 (1985).
[29]P. Pelce and P. Clavin, Europhys. Lett. 3, 907 (1987).
[30]G. K. Batchelor, J. Fluid Mech. 184, 399 (1987).